

Multispectral Snapshot Imagers Onboard Small Satellite Formations for Multi-Angular Remote Sensing

Sreeja Nag, Tilak Hewagama, Georgi T. Georgiev, Bert Pasquale, Shahid Aslam, *Member, IEEE*, and Charles K. Gatebe

Abstract—Multispectral snapshot imagers are capable of producing 2-D spatial images with a single exposure at selected, numerous wavelengths using the same camera, therefore, operate differently from push broom or whiskbroom imagers. They are payloads of choice in multi-angular, multi-spectral imaging missions that use small satellites flying in controlled formation, to retrieve Earth science measurements dependent on the target's bidirectional reflectance-distribution function. Narrow fields of view are needed to capture images with moderate spatial resolution. This paper quantifies the dependencies of the imager's optical system, spectral elements, and camera on the requirements of the formation mission and their impact on performance metrics, such as spectral range, swath, and signal-to-noise ratio (SNR). All variables and metrics have been generated from a comprehensive, payload design tool. The baseline optical parameters selected (a diameter of 7 cm, a focal length of 10.5 cm, a pixel size of 20 μm , and a field of view of 1.15°) and snapshot imaging technologies are available. The spectral components shortlisted were waveguide spectrometers, acousto-optic tunable filters (AOTF), electronically actuated Fabry–Perot interferometers, and integral field spectrographs. Qualitative evaluation favored AOTFs, because of their low weight, small size, and flight heritage. Quantitative analysis showed that the waveguide spectrometers perform better in terms of achievable swath (10–90 km) and SNR (>20) for 86 wavebands, but the data volume generated will need very high bandwidth communication

to downlink. AOTFs meet the external data volume caps well as the minimum spectral (wavebands) and radiometric (SNR) requirements, therefore, are found to be currently feasible in spite of lower swath and SNR.

Index Terms—Small satellites, BRDF, imager design.

I. INTRODUCTION

MULTI-ANGLE, multi-spectral remote sensing is very important for many earth science remote sensing applications [1], for example, the derivation of surface albedo, calculation of radiative forcing, land cover classification, cloud detection, atmospheric corrections, and aerosol optical properties. Bidirectional reflectance-distribution function (BRDF) is a theoretical, geometric representation of the reflecting properties of a surface element [2] and therefore a key parameter in the interpretation of multi-angle remote sensing. BRDF can be determined from multi-spectral measurements that involve tiny but non-zero changes in illumination and reflectance angles. BRDF of a ground spot can be estimated from air or space, using multiple images over the same area viewed from different directions at a specific angle of solar illumination. Previous simulations and literature have shown that multiple small satellites, in controlled formation flight, can simultaneously image a ground spot at multiple 3D angles at the same time as they pass overhead [3]. These measurements can retrieve BRDF more accurately than single satellites with multiple view angles that sample different spatial footprints, but do not view a given footprint from different lines-of-sight simultaneously [4]. The payload or primary sensor on each satellite in such a formation will be a small snapshot imaging spectrometer that measures narrow-spectral-band reflectance in the FOV. This medium-resolution snapshot imager has a narrow field-of-view (NFOV) within a few degrees. The pointing requirements for a mission with NFOV payloads are relatively strict because all the satellites have to point their NFOV payload toward the same ground spot at approximately the same time to construct the multi-angle image. If push broom spectrometers (e.g., based on discrete or linear variable filters) are used, only a single row of pixels will be available in the nadir direction and an error equal to the instantaneous field of view (iFOV) would lead to the loss of one angular measurement. For example, if the iFOV is 0.1°, then a satellite's nadir error of 0.1° may cause that satellite to miss the common ground target. This pointing risk may be reduced by the use of hyperspectral

Manuscript received March 30, 2017; accepted June 13, 2017. This work was supported in part by the Schlumberger Faculty for the Future Fellowship and in part by the MIT Zakhartchenko Fellowship. The associate editor coordinating the review of this paper and approving it for publication was Prof. Kazuaki Sawada. (*Corresponding author: Sreeja Nag.*)

S. Nag was with the Massachusetts Institute of Technology, Cambridge, MA 02139 USA. She is now with the Bay Area Environmental Research Institute, Petaluma, CA 94952 USA, and also with the NASA Ames Research Center, Mountain View, CA 94035 USA (e-mail: sreejanag@alum.mit.edu).

T. Hewagama is with the University of Maryland, College Park, MD 20742 USA, and also with the Planetary Systems Laboratory, NASA Goddard Space Flight Center, Greenbelt, MD 20771 USA (e-mail: tilak.hewagama@nasa.gov).

G. T. Georgiev was with the NASA Goddard Space Flight Center, Greenbelt, MD 20771 USA, and also with the University of Maryland, College Park, MD 20742 USA. He is now with the Electro-Optic Sensor Systems, NASA Langley Research Center, Hampton, VA 23666 USA (e-mail: georgi.t.georgiev@nasa.gov).

B. Pasquale is with the Instrument Systems and Technology Division, NASA Goddard Space Flight Center, Greenbelt, MD 20771 USA (e-mail: bert.a.pasquale@nasa.gov).

S. Aslam is with the Solar System Exploration Division, NASA Goddard Space Flight Center, Greenbelt, MD 20771 USA (e-mail: shahid.aslam-1@nasa.gov).

C. K. Gatebe is with the Climate and Radiation Branch, NASA Goddard Space Flight Center, Greenbelt, MD 20771 USA, and also with the Universities Space Research Association, Columbia, MD 21046 USA (e-mail: charles.k.gatebe@nasa.gov).

Digital Object Identifier 10.1109/JSEN.2017.2717384

or multi-spectral snapshot imaging, which produces 2D spatial images with a single exposure by the same camera at design wavelength bands. Previous literature [5] has proven in simulation that current, commercial attitude control systems for small satellites allows for more than 80% overlap between the ground spots, when snapshot imagers are used, for spacecraft attitude determination control better than 0.5° and position determination error better than 2 km.

Multi-spectral snapshot imaging can be understood as obtaining 2D spatial images, where in spectral content of each pixel is also captured (1D spectral), without the need of separate cameras or telescopes for different wavelengths. It is thus also called 3D imaging. Since the formations will need multiple snapshot imagers, it is in the interest of cost, launch and maintenance efficiency to make them small, light weight and low power. Nano-satellite spectrometers and snapshot imagers have been demonstrated, however they have only recently been integrated as payloads, for space applications in the laboratory. For example, Space Dynamics Lab is developing OPAL, a snapshot hyperspectral instrument with very high spectral resolution and tradeoffs with respect to bandwidth and horizontal sampling [6], covering the visible spectrum. Existing spectral imagers for BRDF estimation have traditionally been very large and CHRIS onboard *Proba* was the lightest multi-angular imager (~ 14 kg). The radiometric precision, image quality and SNRs of the small imagers are not expected to be similar to the heritage instruments. However, the images are required to have SNR high enough to distinguish between signals captured by different satellites, so that the relative reflectance difference between the multiple angles is accurately characterized. These observations may then be complemented with high quality data from heritage missions, producing a database which includes angular information at higher accuracy than before.

Theoretically popular methods for snapshot imaging are: (i) computerized tomography to calculate the 3D input (x, y, λ) from the 2D output image on the Focal Plane Array (FPA) at multiple diffraction orders [7], [8]; (ii) image slicers made of appropriately aligned mirrors and grisms to slice the 2D spatial image into a 1D vector and then disperse it spectrally [9]; (iii) multiple apertures at the input lens [10] followed by a dispersive or a spectral element such as a Fabry-Perot filter array [11] and (iv) birefringent interferometers for spectral filtering by two-beam interference, followed by spatial/spectral demultiplexing by passing the light through a Wollaston prism [12]. The tomographic approaches suffer from difficulties in inverting complex waveform equations unless the SNR is very high. Image slicers typically need cryogenic temperatures (the modern version of the Bowen slicer has demonstrated otherwise), which need high mass and power. Fiber optic reformatters are preferred at visible and near infrared (VNIR) wavelengths [13] only. Multiple apertures severely restrict the spatial FOV and thus ground resolution, unless multiple large telescopes are accommodated. Snapshot imagers have also used the concept of wavelength tunable filters [14], for example, Liquid Crystal Tunable Filters (LCTF). A Lyot-Ohman type LCTF which consists of a stack of polarizers and tunable retardation (birefringent) liquid crystal plates

has been used in imaging instruments in the VNIR wavelength range. Liquid crystals however are limited by the relaxation time of the crystal - in the range of 40-60 ms [14] - which is much too slow for many applications that require fast switching of pass band wavelength to accommodate all wavebands within the available integration time and a quicker alternative is the Bragg Tunable Filter (BTF) [15].

The size, weight and power constraints of nanosatellites, or nanosats, make the above 3D imaging technologies inappropriate for use in BRDF formation flight. Nonetheless, starting with SwissCube [16] in 2009, nano-satellites payloads have gone beyond technology and educational demonstrations and attempted to make scientific contributions in Earth Remote Sensing. VNIR hyperspectrometers for small satellites have been successfully demonstrated in Japan's "Taiki" [17] using a Ritchey-Chrétien telescope and commercial-off-the-shelf (COTS) charge coupled device (CCD) image arrays. Aalto-1 is a 400g spectral imager based on a tunable MEMS and piezo-actuated Fabry-Perot Interferometer developed by Aalto University in Finland. The Can-X series of nanosats have carried spectrometers, Cloud CubeSat a VNIR camera and a polarimeter, and QuakeSat a ULF signal sensor [18]. All these successful remote sensing, nanosats have paved the path for the miniaturization of telescopes, adaptation of CCD or complementary metal-oxide-semiconductor (CMOS) arrays for Cubesats and usage of simple dichroic filters or gratings to disperse the different wavelengths of incident light instead of using movable parts.

This paper establishes the requirements for VNIR snapshot imagers that can be used on nanosatellite formations to retrieve multi-spectral, multi-angular images of ground spots and thereby enable spatial, spectral, and radiometric sampling of the BRDF. Owing to the complexity of a satellite formation, its imager (payload) modeling involves many trades. For example, the signal strength and ground sample distance drops as the satellite points off-nadir or is at a higher altitude, overlap between the co-registered images by different satellites in the formation reduces with increased pointing and position errors and signal strength varies over the spectral range of interest. Images from different spacecraft can be processed separately, however will need to be co-registered to compute overlapping sections that will serve as the final, multi-angular image. The technical feasibility of developing such a 3D imaging payload using COTS components and existing spectrometer technologies has been evaluated and a few high-level components suggested. The full tradespace of system design variables of the satellite formation relevant to the VNIR sensor has been explored, and key payload performance metrics as a function of changing design variables simulated.

II. MODELING AND SIMULATION METHODOLOGY

High-level modeling of the payload (a multi-spectral snapshot imager) is important to not only identify the COTS components and technology feasibility, but also to quantify performance metrics in the spatial, spectral sampling dimensions. Our trade study identifies basic optics, dispersive/diffraction elements, their parameters, and compares the identified choices qualitatively and quantitatively, in terms of several system

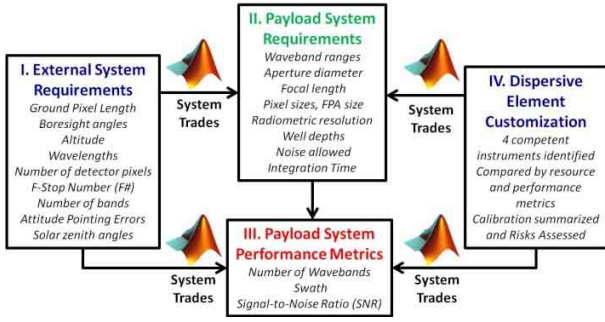


Fig. 1. Summary of the modeling approach to design and evaluate multispectral snapshot imagers for nano-satellite formations performing multi-angular Earth observation. Tradespace analysis of the spectrometer payload allows for mapping the effect of changing external requirements (Box I) and available spectroscopic technologies (Box IV) on the optical system (Box II) and performance metrics (Box III). The model is implemented in MATLAB.

performance metrics. Detailed imager designing will be performed in Phase B-level future work.

Figure 1 shows the payload tradespace exploration model that will be used to calculate the dependence of the spatial and spectral metrics on the measurement requirements, technology constraints and angular range. More specifically, it is used to estimate the dependence of the payload system requirements (Box II in Figure 1) and the system performance metrics (Box III) on the external system requirements (Box I) and on the spectral element design (Box IV). The external system requirements are obtained from either BRDF science requirements derived from heritage airborne missions [19] (e.g., wavelengths, number of bands, ground pixel size), from orbital geometry (e.g., altitude, boresight angles) and from capabilities of nanosat technology (e.g., available telescopes, iFOV and FOV, attitude pointing errors, communication radios). These serve as measurement requirements which map to optical system requirements. These requirements impose design constraints on a miniaturized spectrometer. The spectrometer system performance metrics are established *via* functional test (technical performance checks) and form mapping (nanosat bus fitting checks). Finally, four spectral or dispersive elements suitable for snapshot imaging by nanosats have been proposed, along with detector arrays of CCD, Si, or InGaAs diodes. The spectral/dispersive elements will be compared to each other based on spectral performance, resource cost and impact on system performance. The tradespace analysis goals within this paper are to optimize the performance metrics: maximize swath so as to increase the overlap of ground spots of all satellites; obtain as many channels as possible, as informed by the Cloud Absorption Radiometer (CAR) [19] spectral range; and maximize SNR for improved quality of images.

A. Measurement Goals and External System Requirements

The requirements for the mission are derived from state-of-the-art spaceborne instruments and airborne instruments currently used for BRDF estimation [4, Table 1] and described comprehensively in [3]. The ground sample distance of the detector pixels is limited to a maximum of 500m [3]. The satellite altitudes are restricted to low Earth orbit (LEO) for this analysis. The off-nadir and azimuthal angles of measurements are constrained by attitude control abilities of

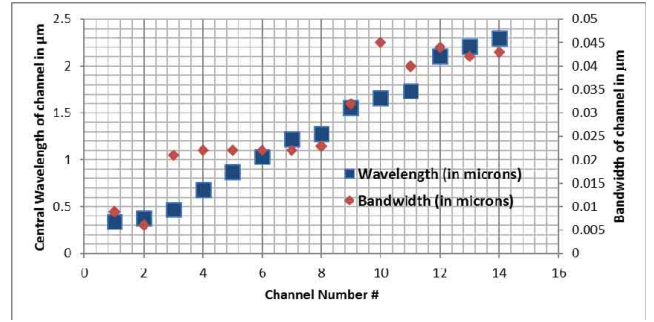


Fig. 2. Wavelength requirements for the imaging spectrometer based on the Cloud Absorption Radiometer airborne instrument at NASA GSFC [19].

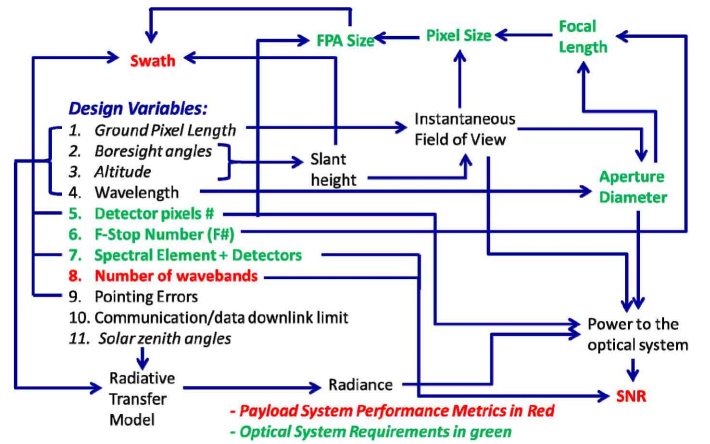


Fig. 3. Dependency chart of payload system performance metrics (red) and optical system parameters (green) on the design variables, which includes external system requirements, customized spectral components and the FPA detectors. Each arrow represents equations. The variables in *italics* are inputs from the external orbital mechanics model, described in [3].

nanosatellites within LEO disturbances [5], thus off-nadir look angles are restricted to a maximum of 60°. Measurements will be collected over all solar illumination angles but only during daylight because BRDF has physical significance only in the VNIR (near solar) spectrum. Data generated per day by any satellite is limited to that which can be downlinked using any of the 12 global NASA Earth Network ground stations using commercially available Cubesat S- or X-band radios [20].

Specifically, the spectral requirements for the mission are derived from CAR, NASA GSFC's heritage BRDF instrument, which makes hundreds of thousands of angular measurements of local spots by flying around them in circles at different altitudes [19]. The CAR spectral bands centers and widths (summarized in Fig. 2) will be the reference design goal. The array format (<2k pixels per detector side), F-number (F# <7.0), and spectrometer characteristics have been chosen to fit within volumetric constraints of 6U CubeSat bus architectures by ample margin. VNIR cameras with up to 10k pixels per side are now available commercially.

B. System Level Optics Modeling and Payload System Requirements

The high-level payload evaluation model has been graphically represented in Figure 3. The design variables are derived from external requirements and technologically viable spectroscopic systems (Figure 1-Box I and IV). The green variables

$$R = \frac{\Delta\lambda}{\delta\lambda} = \frac{BandWavelength_{UpperBound} - BandWavelength_{LowerBound}}{Bin_width} \quad \text{Equation 1}$$

represent simulated optical system requirements and the red parameters the simulated performance metrics to be used to compare different payload system architectures. Each arrow represents a quantitative relationship between connecting variables and parameters. For example, swath is a function of optical FOV (spot) size, slant height, and attitude pointing errors. In this paper, we have assumed that the FOV spans the sensor focal plane array.

The spectral range of BRDF interest is divided into sub ranges or bands – of width $\Delta\lambda$ as per Equation 1, as shown at the top of this page. Each band is spectroscopically characterized by multiple bins with nearly uniform width ($\delta\lambda$ in Equation 1) corresponding to spectral resolution. The number of bins in a band is given by R in Equation 1.

The required instantaneous field of view (iFOV) capable of mapping to a given ground pixel size (gps) depends on the boresight inclination to nadir (η), and altitude (H). D is the slant distance between the sensor and the ground pixel and dependent on H , η , ε , the elevation angle and ρ , the boresight angle at the horizon. Unless mentioned otherwise, all relationships are quantified using well-known equations [21]. The pixel size required to capture at least one ground resolution element is the product of iFOV angle and focal length (f). A pixel size can be selected depending on the altitude, viewing angle and ground resolution needed (\overline{dp} in Equation 2) – for diffraction limited imaging only. The swath achieved by the instrument can then be calculated as a function of its focal length (f) and number of cross track pixels of the focal plane array ($npix$) per Equation 2. \overline{dp} or pixel size with length units, is selected as a value lower than dp (gps, H , η) = iFOV (gps, H , η) * f .

$$swath = \frac{D(H, \eta)}{f} * npix * \overline{dp} \quad \text{Equation 2}$$

The total power received on the FPA is calculated using the solid angle (converting FOV to solid angle in steradians), projection to the normal, and the clear aperture surface area:

$$P(\lambda, \eta, h, SZA) = L(\lambda, \eta, SZA) * BW(\lambda) * \left(\pi * Da * \sin\left(\frac{FOV}{2}\right) \right)^2 \quad \text{Equations 3}$$

where FOV = the full field of view achievable using the entire focal plane array, Da = aperture radius, $BW(\lambda)$ is the width of the spectral bin at λ and $L(\lambda, \eta, SZA)$ (the bin integrated radiance) is obtained from radiation transfer models. This power, modulated by the optical transmission of the spectrometer, reaches the detectors on the FPA. While instrument optical efficiency varies with the spectrometer type, a fixed conservative value of 0.5 has been used for this model. Energy received at the FPA is the integration of power received over the exposure or integration time of one image (intTime) per Equation 4. Integration time is a subset of the dwell time available to the sensor over any ground pixel (gps) for any

given altitude (alt) and spectral element type.

$$E = P(\lambda, \eta, h, SZA) * intTime(totalPixels, nbands, tuningTime, readoutTime, spatialPixels, gps, alt) \quad \text{Equations 4}$$

The noise (N) components depend on the detectors and electronics selected, signal received and stray light. We have assumed CCD detectors - Equation 5 – where N_* is the total number of signal photons (S). The major contributors of noise are readout noise N_R , dark current noise N_D and random sky noise N_S . Readout noise is assumed to be $5 e^-$ (for 16 bit A/D at 1 MBPS readout), dark current $12.5 e^-/pixel/s$ [22] and random noise at the detector ~ 300 electrons [23].

$$\frac{S}{N} = \frac{N_*}{\sqrt{N_* + npix(N_S + N_D + N_R^2)}} \quad \text{Equations 5}$$

SNR given by Equation 5, is considered the main determinant of multi-angle image quality in this study. Heritage instruments typically have an SNR requirement over 100; for example, SNR of 200 for the airborne AVIRIS instrument [24] and 250 for CHRIS [25]. On the other hand, an SNR of as low as 5-10 has in the past provided useful data when used with appropriate algorithms [26] and MODIS considers up to 5% uncertainty in its data as acceptable. This paper focuses less on absolute SNR and more on how the external variables and spectral components in Figure 19 impact the SNR among the satellite formation. Therefore, SNR 20 is taken as a soft requirement. The modeled SNR is sensitive to quantum efficiency (QE) as a function of wavelength (here a worst-case value of 0.5, over the covered spectral range, is used [27]) and the worst-case charge transfer efficiency (CTE) of the CCD is assumed to be 0.99.

III. SPECTRAL ELEMENT OPTIONS AND CUSTOMIZATION

Heritage spectrometers have traditionally been based on prisms, diffraction gratings, filters, heterodyne-mixers, and interferometers (Fabry-Perot, Fourier transform). Slit based dispersive devices (*i.e.*, prisms, gratings) are best applicable for imaging a vector of spatial elements multi-spectrally. Grating spectrometers employ a push-broom method to accumulate a 2D image over time. However, the dispersive nature of such devices prevents their use as snapshot imagers because one dimension is consumed by the dispersed spectrum [28]. We reviewed contemporary literature on multi-spectral snapshot imagers and have identified four possible snapshot imager designs appropriate for nanosatellites in multi-angular formations. While traditional Sagnac spatial heterodyne interferometers [6] may also be used, they have not been discussed below because the methods to evaluate them are similar to those used for waveguide (WG) spectrometers.

A. Photonics Waveguide Spectrometers

Fourier-transform spectrometer (FTS) devices offer throughput advantages compared to dispersive devices but they typically involve mechanical modulation of the optical path. Spatial heterodyne spectrometers (SHS) are a static implementation of the classic Michelson interferometer in one of two ways – using gratings or using waveguides. In the first method, the two Michelson mirrors are replaced by diffraction gratings that result in a spatially distributed interferogram. The second method adopts waveguide structures implemented as Mach-Zehnder interferometers (MZI). Multiple waveguide based MZI structures with varying path delays respond to the spectral characteristics of the incident light similar to mirror modulation. The photonics light-wave circuit (PLC) structures generate the interferogram simultaneously [29]. Their advantages include miniaturization of spectrometers, exclusion of moving parts, internal vibration suppression, low power requirements, shock resistance and easy radiation-hardening [30], [31]. The waveguide based spectrometers are popularly coined as “Spectrometers on a Chip”, with further maturation they will be ideal payloads for nanosatellite formation observations.

The radiation received at every spatial pixel in the 2D FOV is delivered to an FTS chip in an ensemble. The incident light illuminates an ensemble of PLC strands. Each strand divides into two arms, and is recombined. The path length difference in the arms is controlled to simulate MZI function in the strand. The MZI structures in the ensemble have varying path differences to simulate phase delay in a mechanically modulated Michelson interferometer. The recombined beams in each MZI interfere at the detector commensurate with the path difference. Thus, the spatially organized MZI structures and detectors measure an interferogram which forms a Fourier transform pair with the original spectrum. The spectral information is encoded in the interferogram samples, and a Fourier transform returns the original spectrum [32]. Calibration errors can also be calculated using linear regression applied to interferogram points for a matrix of path delays. Advantages of waveguides of gratings are the large optical throughput for the same spectral resolution because of the lower probability and intensity of ‘crosstalk’ between the different waveguides [33], ability to calibrate theoretically for ideal path delay and through simulations for non-ideal delay [32] and ability to correct interferometric defects in the post processing phase [30]. The main performance criteria are spectral range and resolution, optical crosstalk, optical loss and polarization wavelength dependence. Visible and near-infrared devices have been reported by researchers [33], [34]. NIR and mid-IR devices are in development phase in NASA GSFC [31].

If the length or path differences of the waveguides vary linearly from 0 to L_{\max} , the number of waveguides needed is given by Equation 6 where $\Delta\lambda$ is the spectral range of the spectrometer, $\delta\lambda$ is the spectral resolution and R is the number of wavelength bin elements or resolution, as defined in III-B. k_0 is the wavenumber and n_{eff} is the mode effective index. For a FTS type device, L_{\max} is a function of

resolution, central wave number, efficiency, number of waveguides needed [34] (Equation 7).

$$N = 2 \frac{\Delta\lambda}{\delta\lambda} = 2R \quad \text{Equation 6}$$

$$L_{\max} = \frac{R}{k_0} \frac{2\pi}{n_{eff}} \quad \text{Equation 7}$$

While FT spectrometers without moving parts have been developed and flight-tested for UV (SHIMMER [35] launched in 2007) and IR wavelengths (SHOW [36] not launched yet), PLC technology readiness level (TRL) is estimated to be between 5 and 6, and methods are being developed to eliminate crosstalk between adjacent waveguides which is estimated to increase with decreasing bandwidth [34].

Transmission bandwidth and the ability to fabricate the optical circuits have been successfully solved [30], [37], [38] but practical implementation in the UV/VIS spectral region do involve significant technical hurdles and trades. Reference [4] discuss losses in a waveguide-based spectrometer as ~ 0.02 dB/cm. The 0.18 numerical aperture of the waveguides subtends a 0.1012 sr solid angle resulting in a system étendue (Area*Solid_Angle) of 1.5×10^{-4} mm² sr. Without coupling losses, this étendue corresponds to a 31” beam on a 80 mm telescope aperture – reasonable in terms of coupling radiation from free space optical systems observing extended sources. For comparison, silica core single mode infrared fibers have comparable numerical apertures (e.g., ThorLabs 1260-1650 nm spectral range single mode fibers with 10e-5 dB/cm). Although the waveguide implementation has substantially higher loss rates, the physical paths (effective optical path is increased by the index-of-refraction) of the waveguides are small and the total losses are sufficiently small for practical use in spectrometers. An alternative technology being considered for the spectrometer is dielectric (solid core) WGs inscribed in IR transmissive devices (e.g., Chalcogenides) using Femtosecond lasers. These structures have low-loss properties in single-mode (6 μ m core) and may be the better alternative. While étendue matching is an issue with fibers/waveguides, beam transforming optics can be used to mitigate such geometric losses. Arrayed Waveguide Grating (AWG) systems, not discussed herein because of throughput and bandwidth trades, are another possible implementation for future consideration.

B. Acousto-Optic Tunable Filter Spectrometers

Acousto-optic tunable filters (AOTF) offer a mechanism to filter broadband incident light by achieving the spectral decomposition in time due to its high spectral agility, and therefore allow multi-spectral snapshot imaging. An AOTF device [39]–[41] can switch from one spectral range to another in the time that it takes an acoustic wave to traverse a solid state crystal (typically tens of microseconds). An acousto-optic cell is a transparent birefringent crystal excited by a radio frequency transducer. Acoustic waves propagate inside the crystal and create regular spatial variations of the refractive index. Under phase-matched conditions, the acoustic waves produce spatially periodic index-of-refraction perturbations in

the Bragg cell and results in diffraction of the incident light. The conditions favoring diffraction are only satisfied for a particular spectral frequency at a particular incident angle and a particular driving frequency. By controlling the transducer frequency, the spectral frequency diffracted can be selected. Controlling the transducer power allows control of the amount of light diffracted. Typical transducer power is on the order of 3-4 W [39]–[42]. While higher transducer power increases the amount of diffracted light, it also degrades spectral resolution by increasing side lobes of the center frequency. Although a number of birefringent materials have been used for AOTF devices, TeO_2 is a frequent choice due to its high acousto-optic figure of merit and good transmission in the ultraviolet (UV) through visible and infrared (350 - 5000 nm). Other materials include TAS which is transparent to 11 μm , and quartz which is transparent in the UV. The spectral range served by AOTFs is limited by the AOTF tuning element at the low wavelengths and by loss in quantum efficiency of CCD FPA at the high cut-off wavelengths.

AOTFs can be used for snapshot imaging in the following manner: Tune to the first desired band, image a 2D spatial matrix at that band, register photons over the integration time period, read out from the CCD and repeat the process for the next wavelength band until all wavebands are exhausted. While this restricts the integration times as will be seen in trades presented in Section V, AOTFs offer the advantage that only specific wavelengths of interest can be chosen and imaged. The spectrometer mass is as low as 4-5 kg [14]. AOTFs have significant heritage since they were used recently on the Mars Express [43], the Venus Express [44] and also to probe Titan's atmosphere back in 1999 [42] with a TRL estimated at 8-9. TeO_2 has a transmission of $\sim 80\text{-}90\%$ (wavelength dependent). Assuming a typical diffraction efficiency of $\sim 80\%$, the filtered light is $\sim 70\%$ of the incident light. Since the AOTF's are polarization devices, transmission of the unpolarized light entering the aperture is reduced to about 35% of the incident light. Total transmittance is theoretically $\sim 21\%$. Reference [45] cited 20% total transmittance and 35% transmittance for polarized light for the AOTF used in the SPICAM spectrometer on Mars Express mission.

C. Integral Field Spectrograph

An integral field spectrograph (IFS) is suitable for 3D imaging because it can gather spectra at every spatial element in its field of view. Although IFS-type instruments are used primarily in ground-based observatories, including the Keck Observatory in Hawaii, the technology has been demonstrated in spaceflight through the TIGER program using lenslets [9] and through the ARGUS program using optical fibers which connected a hexagonal aperture to a single vector imager [13]. An IFS, using lenslets, is currently being used in the development of the CHARIS instrument (which has been successfully demonstrated on the Subaru Telescope in Hawaii) for small satellites to explore exoplanets.

An IFS simultaneously obtains spatial and spectral information over the field of view by dispersing the entire image on the detector, using lenslets, to sample the image plane [46]. Each lenslet samples a piece of the image and focuses it to

a spot with the energy distribution given by the instrument point spread function (PSF). Each spot is dispersed and then sensed by the multiple detector elements. This allows the IFS to measure two spatial and one spectral dimension simultaneously by spreading the spectrum over multiple spatial pixels and mapping 3 dimensions onto the 2D detector plane. IFS also offers the advantage of low mass and volume as well as a mid-TRL of 5-6. The TRL is lower (3-4) for small satellite payloads, especially for non-astronomical observations. The disadvantage is that each dispersed spectrum for a spatial pixel may take up to 35 detector pixels in length and 6 pixels in width (focused by a lenslet element) [46] causing a significant reduction in the number of pixels available for spatial imaging. Additional beam resizing will be needed to focus the image on the larger pixel, therefore different from the trades shown for WG or AOTF images, adding more volume. Finally, processing shown to de-convolve the spectral and spatial data from the same detector array may be complex.

There are snapshot mosaic cameras available commercially such as the XIMEA xiSpec (<https://www.ximea.com/>), which uses Imec sensors. These CMOS visible-NIR cameras integrate hyperspectral filters (Fabry-Perot) at the wafer-level producing a spectrometer on chip scale devices. Current technology produces images across ~ 25 wavebands below $1\mu\text{m}$ that can be imaged onto the same array, allowing ~ 170 cubes/s. The spatial extent of the image can be improved if the wavebands are tunable, and can be imaged one at a time, as described below.

D. Electronically Actuated Fabry Perot Interferometers

The traditional Fabry-Perot Interferometer (FPI) [14] has been used as a tunable filter since its invention. When using an FPI as a snapshot imager, light from the object is collimated by the front optics and the collimated beam is directed to the FPI cavity and order-sorting filter. This combination passes only one narrow wavelength band, determined by the air gap value and the selected FPI order filter. In spite of the optics focusing the light transmitted through the FPI to an object image, the light beam through the FPI is not totally collimated and this has an effect on the spectral resolution of the instrument across the FOV. When low orders of the FPI (1 - 4) are used, the spectral resolution is not dominated by the collimation level of the optical beam as far as the incident angle is below 5° (which is true for our proposed instrument, as seen in Section V).

The air gap value of the FPI and hence the order of FPI can be scanned from 0 to tens of micrometers, by piezo actuators and the images are recorded as a function of air gap width [47]. For each pixel, there is a signal, as function of the air gap value, containing the information of the spectrum of the light entering the FPI. The spectrum of the incident light can be retrieved from the measured signal. This concept has been used for the development of the primary payload of the Aalto-1 CubeSat developed by the Technical Research Centre of Finland [27], [48]. For a selected air gap value, signals of the B-, G- and R-pixels are given by the theoretical spectral responses or transmittances integrated over the waveband. COTS multispectral sensors

for the UV and VNIR ranges can easily be obtained from Ocean Optics Inc. (<https://oceanoptics.com/>) and Silios Technologies (<http://www.silios.com/>). The total operating range is 400 – 1100 nm and spectral sampling below 1 nm is possible for a stability of 0.1 nm. Time required to change the wavelength band is less than 2 ms, $F\# < 4.0$ is supported along with a full FOV up to 20° . The entire instrument fits within a 110 mm \times 75 mm \times 55 mm envelope, weighs less than 350 g and consumes an average of 3W.

IV. RESULTS FROM MODELING AND SIMULATION

This section presents results from modeling the expected radiation received by the spaceborne instrument, optical system requirements and functional and form comparison between the snapshot imaging spectral elements, as presented in Figure 1 and Figure 3. These preliminary results are used to inform the selection of a few baseline parameters of the optical and dispersive system, which will then be used in the next section, to compute performance metrics as trades across the chief design variables, per Figure 3.

A. Radiative Transfer Modeling for Signal and Noise

SNR is one of the most important metrics for determining the performance of the optical system and can be estimated from radiance at a given altitude over the area of the aperture and integration time, whose upper limit is set by the ground velocity and ground pixel size to reduce image smearing - **Equation 5**. Earth's radiance is calculated using atmospheric radiative transfer models; e.g., SBDART from the UCSB (Santa Barbara DISTORT Atmospheric Radiative Transfer Model) or COART (Coupled Ocean-Atmosphere Radiative Transfer) from NASA Langley, or extracted from spacecraft mission data archives.

In this study, the COART model [49], a publicly distributed software for radiative transfer by NASA, was used to calculate the top-of-the-atmosphere up-welling radiance in $\text{W/m}^2/\text{sr}/\mu\text{m}$ at an altitude of 100 km (above which atmospheric effects are small in this context) for different solar zenith angles (SZA), sensor boresight angle (η) and wavelength of radiation (λ). Figure 4 shows the COART model radiances for $\text{SZA} = 0^\circ$ and 80° in the null azimuth direction with respect to the Sun. With a peak near 500 nm, the TOA radiance shows a decreasing trend for 700-1400 nm or NIR. There is a drop in radiance in the UV and SWIR regions due to characteristic solar TOA spectrum and atmospheric transmittance changes. Increasing SZA angles leads to more outward radiance because the earth radiates more during sunset than noon. The boresight angle dependence is very little compared to dependence on wavelength and SZA, however, it becomes more significant with higher SZA. Also, the COART model has been developed to match available sensor data and since very few missions have successfully sampled the boresight angular variation of radiance, the variation with respect to angles may be underrepresented in these charts.

The numbers are intended only for nominal calculations of expected SNR, to design the payload. Since there is nothing significant to affect the radiation transfer above 100 km,

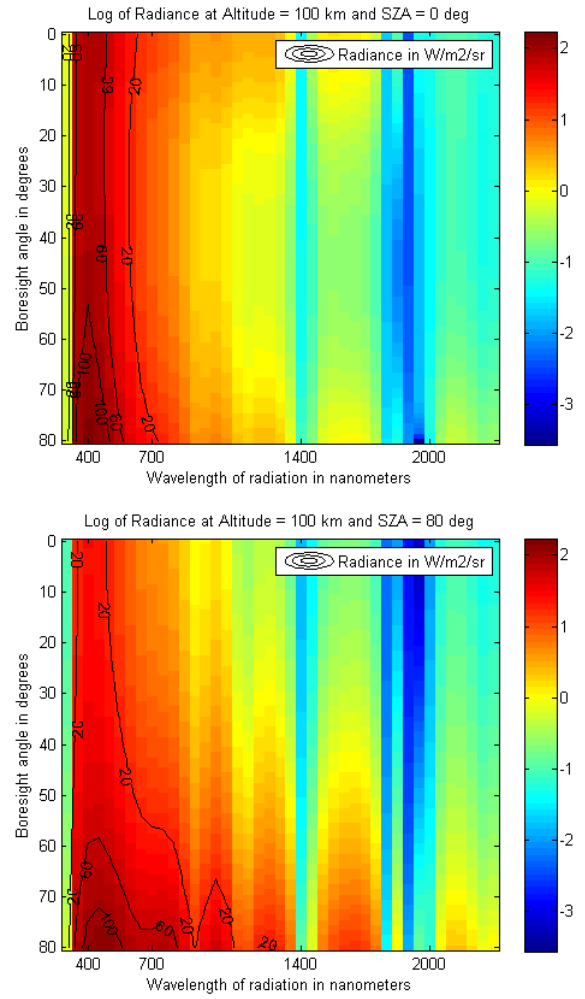


Fig. 4. Radiance per μm at 100 km altitude as provided by the COART model for atmospheric radiative transfer for varying sensor boresight angles and radiation wavelength, for solar zenith angles of 0° (top) and 80° (bottom). The units of the color bar are $\log_{10}(\text{W/m}^2/\text{sr}/\mu\text{m})$ while the contours are in $\text{W/m}^2/\text{sr}/\mu\text{m}$.

the radiance measured at 100 km can be assumed to be the same at LEO altitudes.¹ The COART model results also capture variations of radiance over the time of the day. COART's simulation of atmospheric transmission windows were used as an input to set spectral limits for the wavebands.

B. Mapping the Optical System Requirements

The relationships in Section II-B and Figure 3 can be used to map some of the measurement goals to optical system requirements (green) and metrics (red). Selection of the wavelength bands for the spectrometer depends on the following criteria: (1) Free spectral range of the central wavelength (spacing in optical wavelength between two successive reflected intensity maxima) to prevent spectral aliasing for FTS devices, (2) spectral range of detectors used and (3) radiometric range of detectors used. To prevent the overlap of one dispersive order of a wavelength with the lower order of a higher

¹Confirmed via an email conversation with Dr. Zhonghai Jin, the primary programmer of the COART model

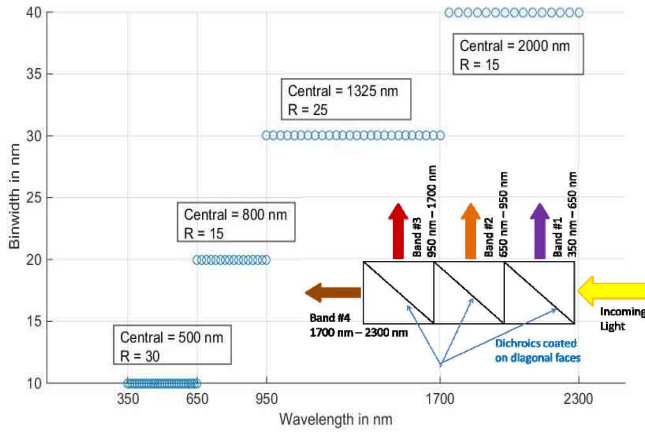


Fig. 5. Proposed wavelength bands for the spectrometer, their corresponding bins and binwidths. The boxes show the central wavelength and resolution or number of bins ($R = \Delta\lambda/\delta\lambda$) for the 4 bands. The inset shows the proposed design for producing 4 wavelength bands for input into 4 spectral components, achievable in a small volume of [1''x0.5''x0.5''].

TABLE I
POTENTIAL WAVELENGTH BANDS AND CORRESPONDING
BINS FOR THE PROPOSED SPECTROMETER

Band #	$\lambda_{\text{lower bound}}$ (nm)	$\lambda_{\text{upper bound}}$ (nm)	Central Wavelength (nm)	Bin-width (nm)	Number of Bins
1	350	650	500	10	30
2	650	950	800	20	15
3	950	1700	1325	30	25
4	1700	2300	2000	40	15

wavelength, each band is restricted to span an octave [28]. Silicon detectors work best between 350 nm to 1000 nm while InGa, InAs or GaAs detectors work best for the NIR to short wave IR range of 1000 - 2500 nm [50]. InGaAs is picked as the detector of choice because it has high D^* (detectivity), low dark current, and responds to spectral range up to 2.3 μm with cooling and is commensurate with CubeSat mass and power requirements. CanX-2 has demonstrated Peltier cooling of detectors on a CubeSat [51]. Mercury-Cadmium-Telluride (MCT, Hg-Cd-Te) quantum detector arrays are another alternative spanning the visible-IR ($\sim 15 \mu\text{m}$) spectral range, but in two focal planes (e.g., visible- $5 \mu\text{m}$ and 5- $15 \mu\text{m}$); MCTs require cryogenic operation. Uncooled microbolometers, like the one demonstrated on the COPPER mission [52], provide solutions to detect from short wave IR ($\sim 1 \mu\text{m}$) ranges to far-IR, however with 10 to 100 times less sensitivity. Thus, COTS detector systems are now available up to $\sim 15 \mu\text{m}$ and micro-cryocoolers for beyond. Detailed payload design in the mission lifecycle's Phase B is required to size the power, volume and thermal resources required to support the cooling technology. All detector FPAs have been modeled in the same way because they do not affect relative trade-off between the performance metrics - swath, SNR and spectral bands possible - for different formation architectures.

Optimizing all the requirements resulted in the wavebands listed in Table 1 and shown schematically in Figure 5. Four wavelength bands are proposed. Incoming light from

into the telescope will be split into these four bands using dichroics as shown in Figure 5's inset. For $f/1.5$, splitting light four ways is very hard to achieve without additional optics for beam shaping and a longer focal length ($f/7$) or two telescopes for the dedicated bands, is more recommended for a CubeSat. Note the bounds and central wavelength of the bands shown in Table 1 define contiguous, non-overlapping bands. Binwidths have been chosen with reference to the CAR instrument (in Figure 2) and to compensate for the drop in radiance energy with increasing wavelength. By design, binwidth within the individual bands monotonically increases with wavelength and longer wavelengths have more spread out spectral bins. The number of bins (R) to be imaged can be calculated from Equation 1 where the variables are listed in Table 1. Since the one-octave-per-band criteria is applicable to only interferometric devices, four bands are required only if FPIs or grating WGs are used as spectral components. PLC WGs, AOTFs and IFS need only two bands, corresponding to different detectors. Signal photons received at the FPA are reduced by a factor depending on the number of splits.

IFOV required for a given ground pixel size clearly decreases with increasing altitude and this is more pronounced at larger nadir angles due to larger increases in the slant distance IFOV required for a given nadir angle increases by relaxing the resolution requirement (ground pixel size or gps). Given the wavelength of radiation and iFOV, the diffraction limited aperture diameter can be calculated. Thereafter, for an $F\#$ of 1.5 (derived from heritage instruments with BRDF products), the focal length and required pixel size can be calculated, assuming at least one detector pixel per ground resolution element at the highest wavelength. For a selected aperture diameter, the diffraction limited spot size for shorter wavelengths will be smaller than larger ones. Therefore, the diffraction limited pixel size calculated from near-IR will cause pixel-limited imaging at UV wavelengths using the same telescope. For different wavelength bands, pixel size also depends on the speed of the camera $F\#$. The number of detector pixels constrains the swath and the focal plane array size.

Since the highest simulated wavelength is 2.3 μm (CAR-based requirement), Figure 6 shows the variation of the required aperture diameter (plotted as \log_{10} to exaggerate the variation for larger ground pixels) and focal length (contoured in bold black) for diffraction limited imaging at altitudes of 500 km and 800 km. Slant distances to the ground pixel (D) have been contoured in plain black. The highest focal lengths and diameters are needed for highest angles, slant distances and resolutions (tightest iFOV requirements), which are the Pareto utopia points. Thus to achieve at least 500 m spatial resolution (NFOV), the diameter can be baselined at $10^{0.85} \sim 7$ cm and the focal length = 10.5 cm for an $F\#$ of 1.5 - which are all feasible within nanosatellite or 6U CubeSat size constraints. The diameter can be increased if the energy simulated through this aperture and thus SNR do not meet the measurement requirements. Square FPAs have been assumed to prevent additional ADCS constraints on aligning an elliptical image on a rectangular FPA.

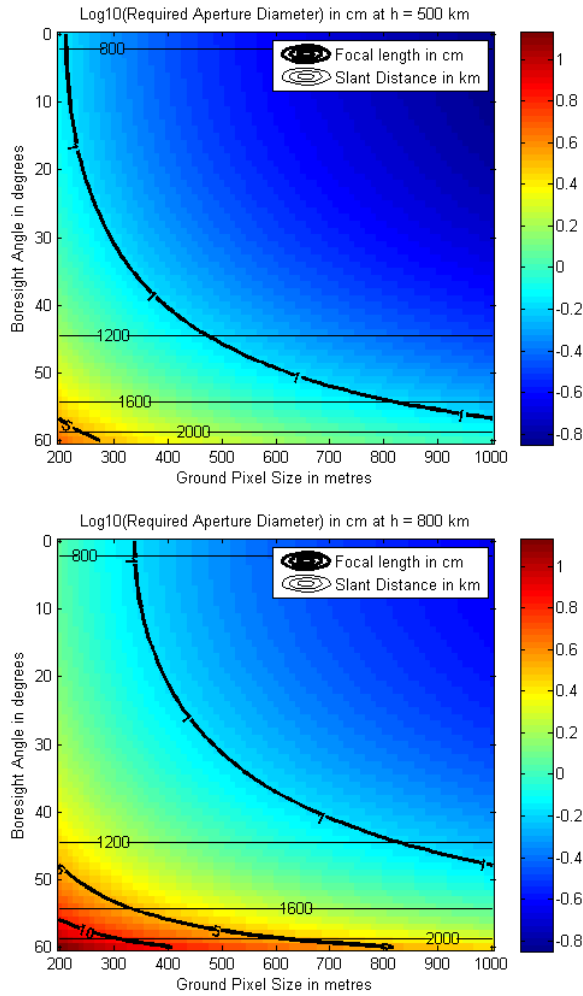


Fig. 6. Variation of required aperture diameter (as log10) at altitudes = 500 km, and 800 km over boresight angle to the ground pixel and ground resolution. The corresponding required focal length (contours) and the slant distances (horizontal lines) for the boresight angles are shown. The worst case boresight angle at 200 m spatial resolution is represented by the bottom left corner, and is the optimum design goal.

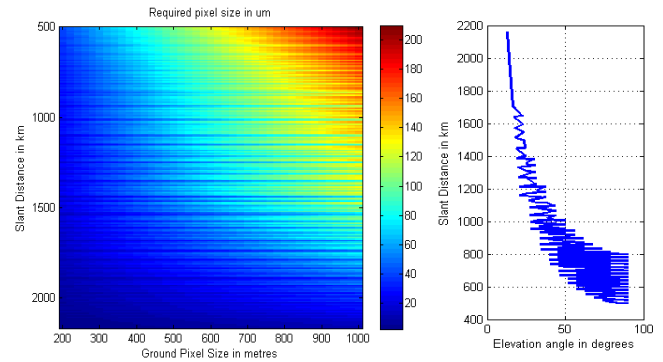


Fig. 7. Required pixel size on the Focal Plane Array (FPA) as a function of slant distance (function of altitude, boresight angle and elevation) and ground resolution. Specific combinations of elevation angles and altitudes result in the same slant distance. The optimum design is represented in the bottom left corner of the left panel.

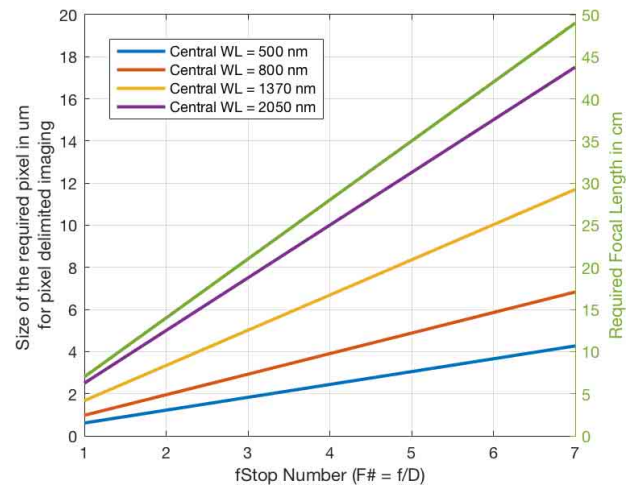


Fig. 8. Dependence of pixel size required to achieve pixel-delimited resolution and focal length on F# for an aperture diameter of 7 cm. For example, f/7 needs a 49 cm focal length.

Assuming the baseline diameter of 7 cm, focal length of 10.5 cm and pixel limited imaging, the required pixel size can be calculated as a function of boresight angle, altitude and ground resolution. Combining the first 2 variables into one, Figure 7 – left panel - shows the required pixel size as a function of slant distance (function of altitude, boresight angle and elevation) and ground resolution. The right panel shows the dependency of slant distance on resolution and satellite viewing, and specific combinations of elevation angles and altitudes result in the same slant distance, therefore the sharp transitions within the curve capturing the same geometric space. The smallest pixels are needed for highest angles, slant distances and resolutions (tightest iFOV requirements). For the required spatial resolution and these extremes, the pixel size can be baselined at 20 μm for diffraction limited imaging at the 2300 nm wavelength.

Since the diffraction limited spot size decreases with wavelength, more resolution is achievable if the pixel size is made smaller for lower wavelengths. Different pixel sizes can

be used for the VIS and IR bands, given that their FPAs will be different. For an f/1.5 system, the maximum pixel sizes required to operate at the respective diffraction limits of the central wavelengths of the four potential instrument bands (500 nm, 800 nm, 1370 nm, 2050 nm), see Figure 8, are calculated to be 1 μm , 1.5 μm , 3 μm and 4 μm , respectively. However, different pixel sizes will project different swaths for the same lens design and FOV, unless denser arrays are used, and pixel limited imaging comes at the cost of swath size. Therefore, we assume equal pixel size for all wavelengths. The longer wavelengths are diffraction limited, the shorter ones are pixel limited and the swath achieved by both are the same. The baselined 20 μm pixel can support pixel limited imaging even at f/7, as confirmed in Figure 8. Smaller diffraction limited pixel than the actual physical pixel reduces blurring and cross talk.

Varying the F# number or the lens speed of the camera changes the required focal length (marked in green in Figure 8) and the required pixel size to resolve up to the diffraction limit of every wavelength range/band (marked in colors in Figure 8).

An F# of 1.5, as assumed in the previous trades, needs a focal length of 10.5 cm which is achievable in 6U cubesats. While a faster lens, can be more ideal for the baseline FOV of 1.15° (FOV confirmed in Section V), freeform optics [53] are capable of imaging as low as 340 nm given a 2° FOV and Paul-Baker telescopes in a multiple-mirror format have been shown to achieve excellent image quality over 1° FOV with an f/1 primary and f/2 final focal ratio [54]. An f/3 to f/7 has been achieved for CubeSats [59] and f/7 will need a 49 cm focal length (Figure 8). Longer focal lengths and higher F# can be possible using a teleconverter or a telephoto lens that reduces the physical focal length, so that the system fits within the payload volume of a CubeSat. Therefore, one may increase the focal length or change other optics specifications (like number of apertures, FPAs, intermediate lens) proposed here to some degree, without critically affecting the relative trade-offs between the spatial and spectral components.

C. Spectral Element Modeling and Comparison

The spectral elements identified in Section III after reviewing possible multi-spectral snapshot imagers are compared below in terms of spectral performance and Cubesat form fitting only. The best option/s are then quantitatively modeled in Section V to compare all performance metrics across all major design variables.

For waveguide spectrometers, the total number of waveguides needed for the spectral ranges in Figure 5 and Equation 6 will be $2 \times 85 = 170$. This number has been demonstrated in the laboratory and published in literature [33], [34]. Reference [55] reports a $8 \mu\text{m}$ pitch between the waveguides, we triple this minimum pitch with the aim of reducing cross-talk and allowing sufficient margin in this preliminary design. The required chip width per spatial pixel is therefore $\sim 5 \text{ mm}$. The required minimum chip length is the basic length of a waveguide (derived from expected losses between spectral input and output) plus L_{max} from III-B [34]. The L_{max} or the path difference for the ranges for the proposed wavelength resolutions and central wavelengths are 0.63 mm, 0.5 mm, 1.39 mm and 1.26 mm for etched glass. Silica is easier to etch but the required precision is more because of the higher resolution of L_{max} . Since PLC WGs are not restricted by the octave constraint, two instead of four wavebands are also sufficient. The thickness of the chip or cradle size, for glass or silica, is less than a 1 mm. Each chip is therefore estimated to be $\sim 5 \text{ mm} \times [0.63 \text{ mm}, 0.5 \text{ mm}, 1.39 \text{ mm}, 1.26 \text{ mm}] \times 1 \text{ mm}$. For example, 25,000 chips will be needed for 25,000 spatial pixels. The chips can be stacked in any way convenient and will occupy a volume less than 160 cm^3 . This compact volume is possible because the Mach Zehnder waveguide strands can be interleaved to reduce the collective volume by 2-3 times compared to the simple stacked layout [33]. Technical challenges involved in fabricating such path differences may be relaxed with the use of high refractive index materials as dielectric substrates. The electronics associated with the operations weigh less than 0.7 kg and the chips are less than a milligram, easily achievable within CubeSat mass constraints.

For Integral Field Spectrographs, an example spatial image of (1000×1000) pixels will require $(35000 \times 6000) = 210$ million pixels on the FPA because the spectral content of each pixel is spread across (35×6) lenslets. Instead, if the required number of spatial pixels is reduced to (50×50) or (107×107) ,² the required FPA pixels is 525,000 and 2.4 million respectively. Additionally, the FPA may need a specific rectangular aspect ratio, so that a regular-sided spatial image can be mapped onto it. For example, a (107×107) pixel spatial image will need $(107 \times 35) \times (107 \times 6)$ pixels on the FPA. While the required number of FPA pixels is high, it is possible to achieve with current FPAs with minimal customization. For example, (107×35) or 3745 pixels on the long side may need commercial FPAs to be stitched together and some extra testing. Given the CHARIS available detector pitch of $18 \mu\text{m}$ (or our baselined detector size of $20 \mu\text{m}$), the FPA will measure at least $6.7 \text{ cm} \times 1.1 \text{ cm}$. Since the aperture diameter has been selected at 7 cm, a similar sized FPA may run into lens curvature errors, and need to increase the aperture diameter or focal lengths. IFS systems will therefore need additional trades against aberrations, including chromatic aberrations, for the fast optical system proposed. Alternatively, one will have to settle for much fewer spatial pixels on the IFS FPA than is available for AOTFs or WGs. Aberrations have not been addressed in this paper because the optics train and FPA is expected to be the same for all spectral components and therefore of little architecture-differentiating value at this stage.

The spectral performance of all four dispersive or spectral elements for snapshot imaging are compared qualitatively below. However, detailed modeling (Section V) is essential for comparing them because AOTFs and tunable FPIs image the spectrum temporally and spectral performance is dependent on and affected by other performance metrics - SNR and swath size. The spectral elements are summarized in Table 2 in terms of their relative fit within nanosatellite resource constraints and the spectral performance. While four can fit within the mass, volume and power requirements of CubeSats, the table shows their relative rank among each other.

The spectral performance metrics we used to compare the four multi-spectral snapshot spectrometers to each other are:

- *Required number of pixels to achieve the same spatial/spectral coverage and resolution:* IFS samples 3D onto a 2D array thus needs the most pixels. WGs image every chip onto the FPA therefore need many pixels as well, however less than lenslets. AOTFs and FPIs sample the spectral dimension in time and therefore relax the requirement of more pixels.
- *Susceptibility to spatial and spectral aberrations:* Since WG spectrometers rely on the Fourier transform of the spectrum, aberrations can be partially but mathematically compensated for [32]. FPI and AOTF avoids such aberrations and has the additional advantage of time domain imaging. IFS runs the risk of overlap of the spatial

²Section V will show that AOTF and WG spectrometers can image 50×50 and 107×107 spatial pixels respectively, on to a 1000×1000 pixel FPA, due to trade-offs in imaging time and SNR

TABLE II

COMPARISON OF THE SELECTED SPECTRAL ELEMENTS IN TERMS OF RESOURCE AND SPECTRAL PERFORMANCE METRICS. THE COLORS INDICATE WHETHER THE EVALUATION IS GOOD (GREEN), ACCEPTABLE (YELLOW) OR BAD (RED) COMPARED TO THE OTHER THREE OPTIONS

Spectrometer Types in terms of Spectral components:	Waveguide Spectrometers [33]	Acousto-Optic Tuning Filters [39]	Integral Field Spectrographs [46]	Tunable Fabry-Perot Interferometers [27]
Spectral Element Resource Metrics:				
Mass	Medium	Low	Medium	Low
Volume	Medium	Medium	Medium	Medium
Power	Low	High	Low	High
TRL	Low	High	Low	Medium
Spectral Element Performance Metrics:				
Required # of pixels	Medium	Low	High	Low
Susceptible to aberrations	Medium	Low	High	Low
Resolution per aperture	High	Medium	High	Medium
Optical Throughput	Medium	Medium	High	Low
Polarization Measurement	Medium	High	Low	Low
Spectral Range	Medium	Low	High	Medium

and spectral components if the lenslet focuses erroneously leading to higher aberrations if not deconvolved correctly.

- *Achievable resolution for the same aperture diameter:* WGs and IFS are flexible to be connected to any telescope. AOTFs have been demonstrated in space with a field stop of 1-2 cm, however the cell can be connected to any large aperture telescope (e.g., >2 m used for imaging Titan [42]) therefore allowing flexibility. Any difference between the cell and telescope aperture can be addressed using focusing optics or beam resizing. Aalto-1's FPI supports a 1.5-2 cm aperture will need to be resized to support the diffraction limit at 7 cm [48].
- *Optical throughput of the full system:* Throughput is expected to be high for waveguide spectrometers if crosstalk is well prevented because they use total internal reflection with minimal loss of energy between the filters and the FPA. To account for the need of beam transforming optics for better étendue matching, WG throughput has been assumed 'medium'. Lenslets in IFS have high throughput without the need of extra optics. AOTFs and FPIs have lower throughput in comparison, because of diffractions or reflections (transmission = 0.1-0.3 [48]), respectively, required to isolate the different wavebands.
- *Possibility of measuring the Stokes' vector or polarization state from the incident light:* Since AOTFs use birefringent crystals, the index of refraction of the "ordinary" axis differs from that of the "extraordinary" axis. By imaging 2 diffraction orders (−1 and +1), it is possible to calculate polarization with some addition to system size. IFS also has the possibility to include polarization [56] but for a much higher addition of pixel numbers than waveguides. FPIs have not demonstrated polarization capabilities yet.
- *Possible spectral range within the UVNIR spectrum:* AOTF crystals are made of TeO₂ which, for practical applications, is transparent shortward of 350 nm.

The CAR airborne instrument has a band of interest at 340 nm which cannot be sampled using AOTFs, unless a bandpass filter is applied for the UV range and quartz is used as the crystal. This alternative requires more transducer power. Aalto-1's FPIs have demonstrated a maximum range up to 1100nm. PLCs are at TRL 5-6 for NIR and MIR ranges of the spectrum, however their rank is limited to 'medium' because of lack of laboratory demonstration for the Visible and UV region. IFS, for a very high number of pixels, can operate in any part of the VNIR spectrum. CHARIS (IFS) can operate in the near infrared ($\lambda = 0.9 - 2.5 \mu\text{m}$) at varying spectral resolution of $R = 14, 33, \text{ and } 65$, hence listed as 'high'.

One specific design out of the above four is difficult to select from qualitative comparison alone. Assuming equal weight and a score of [1, 0.5, 0] for every [green, yellow, red] box in Table 2, normalized averages show that AOTFs emerge at the top with a 65% score followed by waveguides at 55% and FPIs and IFS tied at 50%. Waveguide spectrometers, given 2-3 years of development time and subsequent increase in their TRL, will catch up with AOTFs as a potential candidate. FPIs, have medium TRL sailing on Aalto-1's success, however will still be below AOTF's consistent success in flight heritage. Both AOTFs and FPIs need active power for tuning the spectrometer and are spectrally constrained without increasing power further.

Given current state of art, our qualitative analysis indicates that AOTFs (and then WGs) are most appropriate for the mission in terms of spectral performance. The next section will compare AOTFs and WGs quantitatively and show that WG designs outperform AOTFs in performance trade-offs across spatial and radiometric metrics. FPIs have also been compared when appropriate, because of similar concept of operations as AOTFs. IFS have not been quantitatively compared (for conciseness) but is a very strong candidate for future work.

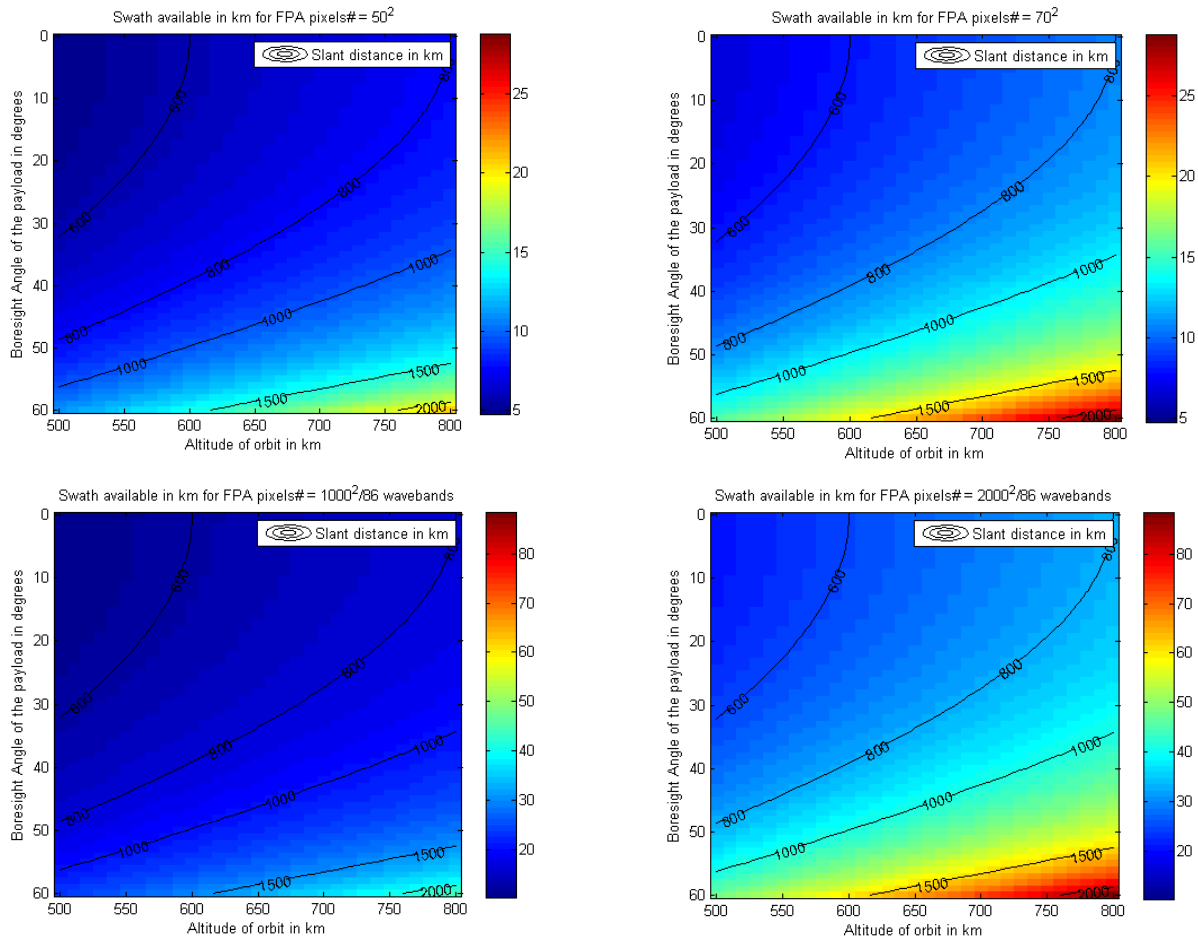


Fig. 9. Simulated swath for an AOTF spectrometer (top row) and a WG spectrometer (bottom row) for a lower (left) and higher (right) number of pixels on the FPA as a function of altitude and varying boresight angles with respect to nadir. The total number of pixels on the WG FPA is shared between 86 spectral bands and actual spatial pixels, which is 107^2 and 215^2 , respectively. All the pixels on the AOTF FPA are available for spatial imaging because the spectral signal is extracted temporally. However, the total number of spatial pixels for the AOTF spectrometer is lower (50^2 and 70^2 respectively) to allow enough time for 14 (minimum requirement) spectral bands.

V. SIMULATED PERFORMANCE OF THE PAYLOAD SYSTEM

This section discusses the payload system performance metrics – swath and SNR – as they vary with the selected design variables and optical system parameters for the selected imagers. The number of pixels on the square FPA is limited to 2000 pixels per side. Previous VNIR nanosatellite missions have used up to 2048 pixels per side [27] and COTS FPAs at (1260×1260) pixels with InGaAs detectors supporting a spectral range up to $2.6 \mu\text{m}$ have been documented in the literature [57]. Integrated, programmable micro-cryocoolers are available for CubeSat cameras (for example, the Ricor K527 cryocooler) and passive cooling COTS systems are sufficient to meet the spectral requirements at lower wavelengths. The baseline case will be (1000×1000) spatial pixels to simulate the most stringent requirements, unless other requirements push the number down further. This corresponds to an FPA side of a few centimeters, which is achievable within nanosatellite optics. Current commercial cameras such as the Hasselblad H6D-100c 100 MP camera, can support $(10,000 \times 10,000)$ pixels, however we present results with 5-10x margin to show value even when using worst-case FPAs. The true swath for a formation of satellites imaging a common ground

target is the overlap of individual swaths of the satellites. Therefore, the true swath is a percentage of the individual swaths, dependent on the control errors of the satellites (dependency listed in **Figure 3**). The swath is wavelength and pixel independent because a constant pixel size suited for diffraction limited imaging ($20 \mu\text{m}$) was assumed.

The swath variation for a given number of pixels on the FPA and spectral element type is shown in Figure 9. The corresponding imager FOV, clockwise from the top left is 0.57° , 1.15° , 2.29° , 1.15° . Swath increases with altitude and with increased look angle *i.e.*, the maximum swath corresponds to near horizon viewing at the maximum satellite-target slant distance. The swath trades for the FPI and AOTF type of spectrometer are nearly identical (therefore only AOTF shown) but very different from the WG spectrometer.

This is because the WGs image all the spectral bands of the 2D ground target at the same time onto the FPA while AOTFs/FPIs, being tuning filters, image the 2D target one band at a time, temporally. The actual number of spatial pixels available to the WG type, given a number of wavebands (nbands), is calculated using Equation 8. AOTF's spatial imaging is time constrained because each waveband has to

be tuned into, imaged, integrated and read out within the time that the satellite flies to the next ground pixel. The spatial pixels available for a given ground pixel size (gps), number of wavebands (nbands), readout time per pixel per image (readoutTime) and tuning time per waveband (tuningTime) is given by Equation 9. Equation 8 and Equation 9 demonstrate the different relationships between spatial and spectral characteristics for the different imager types leading to different payload performances.

$$spatialPixelsWG = \text{floor} \left[\sqrt{\frac{totalPixels}{nbands}} \right] \quad \text{Equation 8}$$

$$intTime + nbands$$

$$* [readoutTime * spatialPixelsAOTF + tuningTime] < \frac{gps}{V_g} \quad \text{Equation 9}$$

At a typical readout rate of 1 megapixel per second, derived to maintain typical output circuit noise to below 5 electrons of noise equivalent signal for a 16 bit A/D, the readout time per pixel is 10^{-6} s. The tuning time per waveband is known to be 10^{-5} s for AOTFs and 2×10^{-3} s for FPIs. For a ground speed of 7.2 km/s ($V_g = \text{function}(\text{altitude})$), ground resolution of 500 m and 86 wavebands to be imaged, the maximum number spatial pixels available to an AOFT imager is (28×28) for a non-zero integration time (Equation 9). A (28×28) pixel array maps to a swath between 5 and 12 km. If the number of required wavebands is reduced to 14, at most (70×70) spatial pixels are available, mapping to a swath up to ~ 30 km. This demonstrates a clear trade-off between spatial and spectral range. The potential number of spatial pixels for the AOTF imager are (70×70) or less (maximum FOV of 1.15°) for at least 14 wavebands (minimum requirement from the CAR instrument in Figure 2). The swath trades for two potential designs – (50×50) and (70×70) – are shown in Figure 9-top panel.

The above analysis (changing pixel number and FPA size) does not take into account any change in lens design, which is usually tightly coupled with FPA size. The same optics (7 cm diameter lens, 10.5 cm focal length) are modeled for changing pixel number and assume that the lens format can be internally optimized to capture all the light for a selected FOV and project it onto a selected FPA size equally efficiently. The lens design will, thus, let a larger FPA capture a bigger image. Since changing the lens design does not significantly affect any of the performance metrics in Figure 1, a simplifying assumption of constant, non-baffled optics is made. The lens diameter is an order of magnitude bigger than any of the considered FPA sizes, so lens curvature is assumed equally insignificant for all the FPA sizes.

As an average-case simulations, the total energy received by a (60×60) pixel FPA is shown in Figure 10 and depends on the wavelength of light, solar zenith angle, altitude and nadir look angle. Equation 3 and Equation 4 have been used to map radiance to energy, integrated over the binwidths shown in Table 1. The tuning time for an AOTF is less than $10 \mu\text{s}$ (FPIs take < 2 ms) so the time taken to tune to 14 spectral bands is < 1 ms. CCD readout accounts for

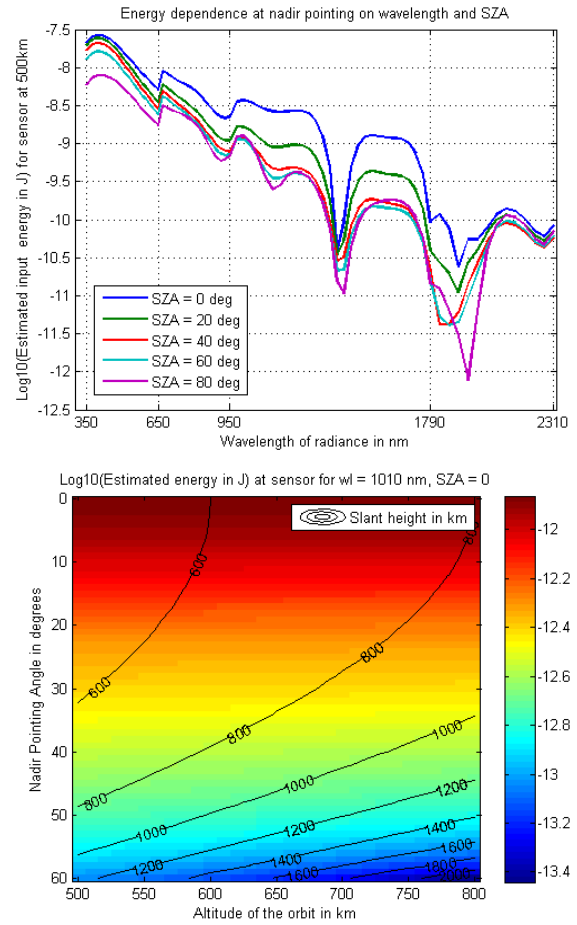


Fig. 10. Simulated energy that reaches the optical system of a snapshot imager with (60×60) pixels as a function of wavelength and solar zenith angle for a nadir looking satellite at 500 km (top) and as a function of boresight pointing angle at 1010 nm at noontime (bottom). Contours mark the slant distance between the satellite and the ground target.

most of the imaging time and the time available for exposure and integration, assuming sequential readout and integration. Therefore, the total number of signal photons are restricted by the number of spatial pixels at 14 bands to be imaged. A monotonic decrease in energy of half an order of magnitude is seen in the visible range of light alone and at any wavelength over the full range of solar illumination angles. The 1010 nm NIR wavelength is chosen (Figure 10-top panel) to demonstrate the variation of power with respect to altitude and boresight angle (Figure 10-bottom panel). The dependence on altitude is negligible compared to angles because COART's simulated radiance is barely affected by small changes in LEO altitudes and slant height.

The dependence of simulated SNRs, calculated using Equation 5 and the associated noise values, on altitude, look angle and wavelength are quite similar for WG and AOTF Spectrometers. However, WG has 100 to 200 SNR more than AOTFs at any given point on the tradespace due to larger number of available spatial pixels and integration time to accumulate signal photons, in spite of imaging 86 bands compared to AOTF's 14. The WG SNR trades are shown in Figure 11. Both instruments show $\text{SNR} > 100$ for all LEO

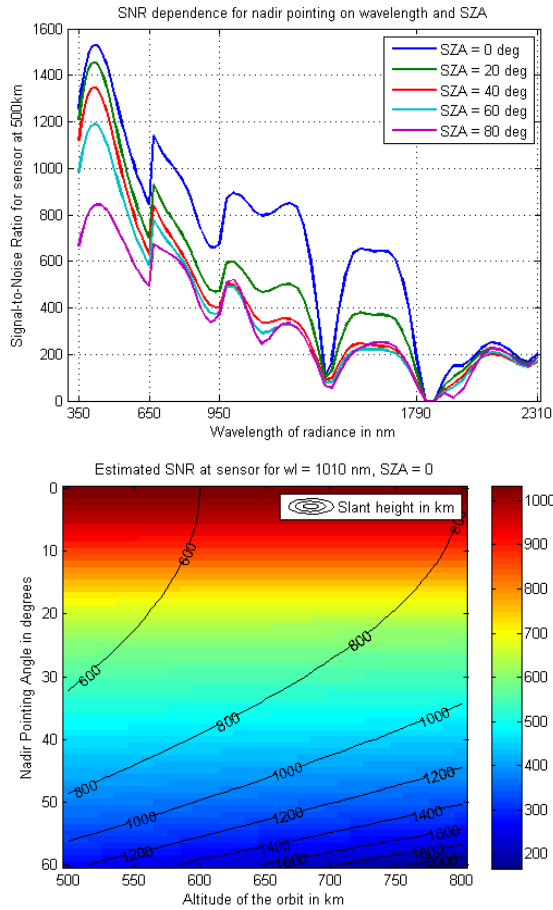


Fig. 11. Simulated SNRs for Waveguide Spectrometers with 1000×1000 FPA pixels as a function of nadir/boresight pointing angle for a wavelength of 1010 nm at noontime (top) and as a function of wavelength and solar zenith angle, nadir viewing at a 500 km altitude (bottom). Quantum efficiency is assumed 0.5, charge transfer efficiency 0.99 and optical transmission 0.5 (all worst case values). Contours mark the slant distance between the satellite and the ground target.

altitudes and view and solar zenith angles for all wavelengths corresponding to atmospheric transmission windows. AOTFs have a unique advantage in their tuning flexibility, that is, 14 discrete and discontinuous bands can be imaged without the need of 14 beam splitters (unlike waveguide FTS which has to image the continuous spectrum). The RF transducer can be programmed to skip the atmospheric block window, which saves a significant fraction of the dwell time and allows the imaging of more spatial pixels for greater integration times, therefore improving SNR. It is this tuning advantage that allows AOTFs to meet the minimum spectral requirements of a BRDF formation flight mission while maintaining a reasonable swath, even if lower than WGs.

To conclude this section, a trade-off between swath, SNR and number of image-able wavebands is quantified for the WG and AOTF spectrometers. These three payload system performance metrics, as identified in Figure 1, are compared in Figure 12 for a wavelength of 1010 nm, nadir viewing during noon from an altitude of 500 km. SNR (color bar) and swath (contours) are plotted in Figure 12 against the required number of wavebands to be imaged and the required ground resolution of the spatial images. The time accounted

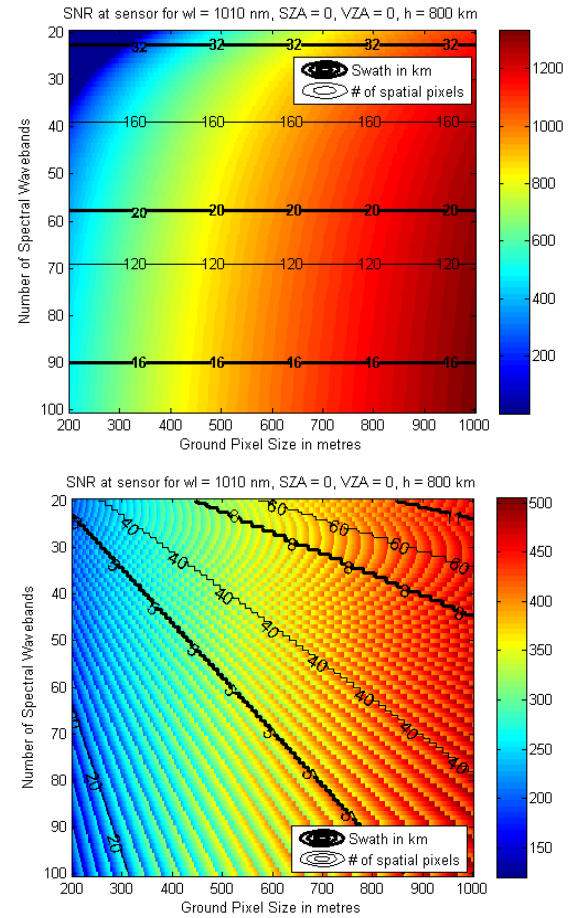


Fig. 12. Simulated SNRs for Waveguide Spectrometers (top) and Acousto-Optic Tunable Filters (bottom) as a function of spectral wavebands and ground resolution required to be imaged for a nadir looking satellite at 500 km, wavelength of 1010 nm, solar incidence at noon and FOV limited to 1.15° . The contours represent the achievable swath (thick black) and the effective number of spatial pixels available on one side of the square FPA (thin black), which are calculated dynamically to maximize swath while allowing at least 5% integration time at a given scene.

for exposure, integration and readout depends on the type of imager, as described before.

For WG spectrometers (Figure 12-top), the number of spatial pixels available simply depends on the number of wavebands required (Equation 8), and linearly impacts the swath imaged. The total number of pixels on the FPA is conservatively assumed to be 1000×1000 with a FOV 1.15° , which is 5-10 times lower than current commercial capabilities thus allowing ample margin. The integration time available increases with the ground pixel size to dwell over, number of wavebands to image before integrating and decreases with number of pixels to read out after exposure. SNR increases or decreases accordingly. For example, increasing wavebands decreases the number of spatial pixels available for imaging, which slightly decreases the readout time required and slightly increases the available integration time and, therefore SNR at the cost of swath.

For AOTF spectrometer (Figure 12-bottom), the number of spatial pixels is maximized in simulation as per Equation 9, such that at least 5% of the total imaging time available is devoted as integration time. The FOV is limited to 1.15° . SNR is then dependent on the available but variable integration

time (IT in Equation 9). The quantum jumps in the SNR chart are due to the constraint on spatial pixels to be integers only. The overall trend shows increased SNR with increased ground resolution required, as with WGs, due to more available integration time. Integration time (above 5% of the dwelling time) and thus SNR increases with decreasing wave numbers. The increase occurs only up to the point where an extra spatial pixel can be fit in, thereby increasing swath at the cost of readout time, at which point the integration time drops to 5% of the dwell time again. This causes the edge like pattern seen in the graph. The results of the above simulation and charts can be used to choose the number of spatial pixels carefully such that the design with the maximum spatial pixels (thus swath) and integration time (thus SNR) is chosen.

Our simulations show that AOTFs achieve lower SNR and swath than WGs for the same number of wavebands, and will not gain as much by using larger or denser FPAs. However, WGs have to image the spectrum continuously, while AOTFs have the advantage of discontinuous spectral imaging and can meet the spectral requirements with lower number of wavebands. Additionally, unless the hyperspectrum is a science requirement, WG spectrometers generate amounts of data that are infeasible to downlink to the NASA Earth Network (NEN) everyday, without Ka or optical bands [20]. For example, the baseline mission is expected to generate 10 Gbits of data per orbit, if WG spectrometers are used, and 3 Gbits, if AOTFs are used. AOTFs can either use X-band links with 3 NEN ground stations or S-band links with 6 or more NEN stations. A potential mitigation strategy for WG devices is to perform onboard Fast Fourier transform processing, band selection, and telemetry of only those bands required by science criteria. WG's quantitative advantages over AOTFs of high SNR and swath are countered by disadvantages of large data volume and low TRL, therefore, both WGs and AOTFs are as potential candidates for the BRDF formation payload.

At the required GSD of 500 m, SNR is >500 for the nadir-pointing satellite using WG spectrometers at 1010 nm and >350 for the same satellite and same wavelength, but using AOTFs (Figure 12). Figure 11-bottom shows a factor of 5 drop in SNR of WG spectrometers when the imager is pointed nadir vs. at a 60° tilt angle, which means that the achievable SNR using a WG spectrometer is at least $\sim 500/5 = \sim 100$ for a maximum tilt of 60° (confirmed through orbit subsystem simulations [5]). Figure 11-top panel shows a factor of 2 drop in SNR from the 1010 nm band to the highest required wavelength of 2300 nm, when atmospheric windows are correctly selected. The worst simulated SNR (at off-nadir viewing) is 100 for WG in VNIR and 50 in Mid-IR. The worst case SNR for AOTFs is lower (70 and 35 respectively), but there is room for improvement if one increases the integration time for the imager. The requirement of SNR 20 is therefore met using the proposed spectral components (WGs and AOTFs) and high-level optics.

VI. SUMMARY AND FUTURE WORK

This paper models a multi-spectral snapshot imager (2D spatial, 1D spectral imager) that can be used as the payload

on each satellite of the BRDF-estimating formation. External system requirements to design a payload for each small satellite have been quantified (for example, ground sample distance or GSD of 500 m) and payload system requirements as well as performance metrics calculated. Baseline optical parameters for NFOV payloads (aperture diameter of 7 cm, focal length of more than 10.5 cm as facilitated by a tele-converter, pixel size of $20\ \mu\text{m}$, field of view of 1.15°) and technologies (for 3D imaging) are shown to lie within state-of-art and commercially feasible. The spectral components shortlisted were WG Spectrometers, AOTFs, electronically actuated FPIs and IFS. Qualitative evaluation favored AOTFs primarily because of their light weight, small size and flight heritage (TRL >6). However, quantitative analysis showed that WG spectrometers perform better in terms of achievable swath (10-90 km) and SNR (>50) for 86 wavebands, but will be more expensive and need much more development and maturation. The different trade-offs between spatial and spectral range for the AOTF versus waveguide spectrometers have been clearly quantified. AOTFs and FPIs (alike), being tunable filters, have the advantage of discontinuous spectral imaging and therefore can outperform WGs if only ~ 14 wavebands are needed, as per science requirements. The time to take one image is restricted to the time the spacecraft takes to travel over 500 m (GSD of the most off-nadir pointing satellite), therefore there is little swath gain in using a larger, denser readout array. The AOTFs take an image every 5 km and the WGs every 10 km, corresponding to the swath width of their reference satellite from a 500 km altitude. IFS has not been discussed herein for succinctness, but will be modeled for future work.

The charts for FPIs are very similar to the AOTF, and the values within the same order of magnitude. The slight differences are attributed to the fact that the waveband switching time is 2 ms (compare to the tuning time of $10\ \mu\text{s}$ for AOTFs). Therefore, the number of spatial pixels allowed for FPI imaging and achievable swath is slightly less than for AOTFs. For example, a maximum of 55 spatial pixels would be image-able for an FPA of (2000×2000) pixels with FPI, which corresponds to a maximum achievable swath of 20 km, as compared to 30 km with AOTFs (Figure 9 top row). The SNRs are similar, and in fact, FPIs have higher SNR than AOTFs by 5-10. Overall, the performance of FPIs and AOTFs is similar with respect to the three metrics considered therefore FPIs have not been discussed in as much detail. The exact waveband number, ground resolution, wavelength and view geometry will be dictated by the geosciences application of multi-angle remote sensing. Nonetheless, SNR >20 has been demonstrated to be achievable using available technologies within CubeSat constraints for all ranges of the above variables. Moreover, if a $10,000 \times 10,000$ pixel camera (e.g. Hasselblad H6D-100c) were used instead of the 1000×1000 baseline we used in this paper and image-collection frequency scaled to fit the available communication bandwidth, the achievable swath can be up to 10 times more.

The 3D imager impacts system performance in terms of swath, thus coverage, spectral and radiometric quality. Future work is required for better understanding of internal trade-offs

such as aberrations, optics speed, number of lenses, cooling strategy, *etc.*, and external disturbances such as temperature, jitter, atmospheric effects, *etc.*, in determining the optimal payload system. Calibration of the spectrometer will be required both pre-flight in the laboratory and also periodically in-flight. Pre-flight calibration is best achieved using integrating spheres available within Goddard's airborne BRDF test facility [58]. In-flight calibration can be performed using white diffuser plates integrated within each sensor, lunar calibration by staring at the moon at the same time and vicarious calibration over pre-selected Earth targets. Inter-satellite calibration of the multi-spectral snapshot imagers is an important consideration because the mission has multiple spacecraft measuring the same target at the same time. This can be done on the ground by comparing calibration data from the different spacecraft and uploading corrections in the next overpass. The proposed imager's potential calibration techniques have been discussed in detail in [20, Appendix X-2].

ACKNOWLEDGMENTS

The authors thank Prof. Olivier de Weck, Prof. Kerri Cahoy, Laura Bayley and Jillian James at the Massachusetts Institute of Technology, Cambridge, MA, USA, for discussions that have significantly improved the quality of this paper.

REFERENCES

- [1] C. K. Gatebe and M. D. King, "Airborne spectral BRDF of various surface types (ocean, vegetation, snow, desert, wetlands, cloud decks, smoke layers) for remote sensing applications," *Remote Sens. Environ.*, vol. 179, pp. 131–148, Jun. 2016.
- [2] F. E. Nicodemus, "Geometrical considerations and nomenclature for reflectance," U.S. Dept. Commerce, Washington, DC, USA, Tech. Rep. 003-003-01793, 1977, vol. 160.
- [3] S. Nag, C. K. Gatebe, and T. Hilker, "Simulation of multiangular remote sensing products using small satellite formations," *IEEE J. Sel. Topics Appl. Earth Observ. Remote Sens.*, vol. 10, no. 2, pp. 638–653, 2017, doi: 1109/JSTARS.2016.2570683.
- [4] S. Nag, C. K. Gatebe, and O. de Weck, "Observing system simulations for small satellite formations estimating bidirectional reflectance," *Int. J. Appl. Earth Observ. Geoinf.*, vol. 43, pp. 102–118, Dec. 2015.
- [5] S. Nag, C. K. Gatebe, D. W. Miller, and O. L. De Weck, "Effect of satellite formations and imaging modes on global albedo estimation," *Acta Astronaut.*, vol. 126, pp. 77–97, Oct. 2016.
- [6] C. Fish, A. Marchant, E. Stromberg, and S. Sullivan, "High performance spectroscopic observation from a CubeSat," presented at the AIAA/USU Conf. Small Satellites, Logan, UT, USA, 2013.
- [7] T. Okamoto and I. Yamaguchi, "Simultaneous acquisition of spectral image information," *Opt. Lett.*, vol. 16, no. 16, pp. 1277–1279, 1991.
- [8] T. Okamoto, A. Takahashi, and I. Yamaguchi, "Simultaneous acquisition of spectral and spatial intensity distribution," *Appl. Spectrosc.*, vol. 47, no. 8, pp. 1198–1202, Aug. 1993.
- [9] R. Bacon *et al.*, "3D spectrography at high spatial resolution. I. Concept and realization of the integral field spectrograph TIGER," *Astron. Astrophys. Suppl. Ser.*, vol. 113, p. 347, Oct. 1995.
- [10] S. A. Mathews, "Design and fabrication of a low-cost, multispectral imaging system," *Appl. Opt.*, vol. 47, no. 28, pp. F71–F76, 2008.
- [11] N. Gupta, P. R. Ashe, and S. Tan, "Miniature snapshot multispectral imager," *Opt. Eng.*, vol. 50, no. 3, p. 033203, 2011.
- [12] A. Gorman, D. W. Fletcher-Holmes, and A. R. Harvey, "Generalization of the Lyot filter and its application to snapshot spectral imaging," *Opt. Exp.*, vol. 18, no. 6, pp. 5602–5608, 2010.
- [13] C. Vanderriest, "Integral field spectroscopy with optical fibres," in *Proc. IAU Colloq. Tridimensional Opt. Spectrosc. Methods Astrophys.*, vol. 71, 1995, p. 209.
- [14] N. Gata, "Imaging spectroscopy using tunable filters: A review," *Proc. SPIE*, vol. 4056, p. 50, Apr. 2000.
- [15] S. Blais-Ouellette, O. Daigle, and K. Taylor, "The imaging Bragg tunable filter: A new path to integral field spectroscopy and narrow band imaging," *Proc. SPIE*, vol. 6269, p. 62695H, Jun. 2006.
- [16] M. Borgeaud *et al.*, "SwissCube: The first entirely-built swiss student satellite with an earth observation payload," in *Small Satellite Missions for Earth Observation*, R. Sandau, H.-P. Roeser, and A. Valenzuela, Eds. Berlin, Germany: Springer, 2010, pp. 207–213.
- [17] S. Satori, Y. Aoyanagi, U. Hara, R. Mitsuhashi, and Y. Takeuchi, "Hyperspectral sensor HSC3000 for nano-satellite TAIKI," *Proc. SPIE*, vol. 7149, p. 71490M, Sep. 2008.
- [18] A. Becerra, M. Diaz, and J. C. Zagal, "Feasibility study of using a small satellite constellation to forecast, monitor and mitigate natural and man-made disasters in Chile and similar developing countries," presented at the AIAA/USU Small Sat Conf., Tech Session, IV, USA, 2012.
- [19] C. K. Gatebe, M. D. King, S. Platnick, G. T. Arnold, E. F. Vermote, and B. Schmid, "Airborne spectral measurements of surface-atmosphere anisotropy for several surfaces and ecosystems over southern Africa," *J. Geophys. Res.*, vol. 108, no. D13, p. SAF25, 2003.
- [20] S. Nag, "Design and evaluation of distributed spacecraft missions for multi-angular earth observation," Ph.D. dissertation, Dept. Aeronautics Astron., Massachusetts Inst. Technol., Cambridge, MA, USA, 2015.
- [21] J. R. Wertz, D. F. Everett, and J. J. Puschell, *Space Mission Engineering: The New SMAD*. Hawthorne, CA, USA: Microcosm Press, 2011.
- [22] M. W. Smith *et al.*, "ExoplanetSat: Detecting transiting exoplanets using a low-cost CubeSat platform," *Proc. SPIE*, vol. 7731, p. 773127, Aug. 2010.
- [23] M. A. Cutter, L. S. Johns, D. R. Lobb, T. L. Williams, and J. J. Settle, "Flight experience of the compact high-resolution imaging spectrometer (CHRIS)," *Proc. SPIE*, vol. 5159, pp. 392–405, Jan. 2003.
- [24] R. O. Green *et al.*, "Imaging spectroscopy and the airborne visible/infrared imaging spectrometer (AVIRIS)," *Remote Sens. Environ.*, vol. 65, no. 3, pp. 227–248, Sep. 1998.
- [25] A. Barducci, D. Guzzi, P. Marcoionni, and I. Pippi, "CHRIS-proba performance evaluation: Signal-to-noise ratio, instrument efficiency and data quality from acquisitions over San Rossore (Italy) test site," in *Proc. 3rd ESA CHRIS/Proba Workshop*, Frascati, Italy, Mar. 2005.
- [26] C. K. Gatebe, T. Varnai, R. Poudyal, C. Ichoku, and M. D. King, "Taking the pulse of pyrocumulus clouds," *Atmos. Environ.*, vol. 52, pp. 121–130, Jun. 2012.
- [27] H. Saari *et al.*, "Novel miniaturized hyperspectral sensor for UAV and space applications," *Proc. SPIE*, vol. 7474, p. 74741M, Sep. 2009.
- [28] E. Loewen and C. Palmer, *Diffraction Grating Handbook*. Irvine, CA, USA: Newport Corporation, 2005.
- [29] P. Cheben, *Optical Waveguides: From Theory to Applied Technologies*, vol. 5, M. L. Calvo and V. Lakshminarayanan, Ed. Boca Raton, FL, USA: CRC Press, 2007.
- [30] N. K. Fontaine, K. Okamoto, T. Su, and S. J. B. Yoo, "Fourier-transform, integrated-optic spatial heterodyne spectrometer on a silica-based planar waveguide with 1-GHz resolution," *Opt. Lett.*, vol. 36, no. 16, pp. 3124–3126, Aug. 2011.
- [31] T. Hewagama, S. Aslam, S. Talabac, J. E. Allen, J. N. Annen, and D. E. Jennings, "Miniature, low-power, waveguide based infrared Fourier transform spectrometer for spacecraft remote sensing," presented at the 9th IAA Low-Cost Planetary Missions Conf., Laurel, MD, USA, 2011.
- [32] M. Florjańczyk, P. Cheben, S. Janz, A. Scott, B. Solheim, and D. X. Xu, "Spatial heterodyne planar waveguide spectrometer: Theory and design," *Proc. SPIE*, vol. 7099, p. 70991L, Jun. 2008.
- [33] K. Okamoto, "Progress and technical challenge for planar waveguide devices: Silica and silicon waveguides," *Laser Photon. Rev.*, vol. 6, no. 1, pp. 14–23, 2012.
- [34] M. Florjańczyk, P. Cheben, S. Janz, A. Scott, B. Solheim, and D. X. Xu, "Planar waveguide spatial heterodyne spectrometer," *Proc. SPIE*, vol. 6796, p. 67963J, Oct. 2007.
- [35] J. M. Harlander *et al.*, "Robust monolithic ultraviolet interferometer for the SHIMMER instrument on STPSat-1," *Appl. Opt.*, vol. 42, no. 15, pp. 2829–2834, 2003.
- [36] Y. Lin *et al.*, "Introduction to spatial heterodyne observations of water (SHOW) project and its instrument development," in *Proc. 14th Int. TOVS Study Conf.*, 2005, pp. 25–31.
- [37] A. V. Velasco *et al.*, "High-resolution Fourier-transform spectrometer chip with microphotonic silicon spiral waveguides," *Opt. Lett.*, vol. 38, no. 5, pp. 706–708, 2013.
- [38] A. V. Velasco *et al.*, "Optical fiber interferometer array for scanless Fourier-transform spectroscopy," *Opt. Lett.*, vol. 38, no. 13, pp. 2262–2264, 2013.
- [39] D. A. Glenar, J. J. Hillman, B. Saif, and J. Bergstralh, "Acousto-optic imaging spectropolarimetry for remote sensing," *Appl. Opt.*, vol. 33, no. 31, pp. 7412–7424, Nov. 1994.

- [40] J. Hillman, D. Glenar, D. M. Kuehn, and N. J. Chanover, "Compact imaging spectrometers using acousto-optic tunable filters," *Weekly News Mag. Sci.*, vol. 155, no. 3, pp. 26–30, 1999.
- [41] G. Georgiev, D. A. Glenar, and J. J. Hillman, "Spectral characterization of acousto-optic filters used in imaging spectroscopy," *Appl. Opt.*, vol. 41, no. 1, pp. 209–217, 2002.
- [42] N. J. Chanover *et al.*, "Probing Titan's lower atmosphere with acousto-optic tuning," *Icarus*, vol. 163, no. 1, pp. 150–163, 2003.
- [43] O. Korabiev *et al.*, "An AOTF-based spectrometer for the studies of Mars atmosphere for Mars express ESA mission," *Adv. Space Res.*, vol. 29, no. 2, pp. 143–150, 2002.
- [44] J. L. Bertaux *et al.*, "SPICAV on Venus express: Three spectrometers to study the global structure and composition of the Venus atmosphere," *Planetary Space Sci.*, vol. 55, no. 12, pp. 1673–1700, 2007.
- [45] O. Korabiev *et al.*, "SPICAM IR acousto-optic spectrometer experiment on Mars Express," *J. Geophys. Res. Planets*, vol. 111, no. E09S03, pp. 1–17, 2006, doi: 10.1029/2006JE002696.
- [46] M. A. Peters *et al.*, "Conceptual design of the coronagraphic high angular resolution imaging spectrograph (Charis) for the Subaru telescope," *Proc. SPIE*, vol. 8446, p. 84467U, Sep. 2012.
- [47] M. Pisani and M. Zucco, "A novel hyperspectral device without moving parts," in *Proc. 7th Int. Conf. Space Opt.*, Tolosa, France, 2008.
- [48] R. Mannila, A. Näsälä, J. Praks, H. Saari, and J. Antila, "Miniaturized spectral imager for Aalto-1 nanosatellite," *Proc. SPIE*, vol. 8176, pp. 817628–1–817628-8, Oct. 2011.
- [49] Z. Jin, T. P. Charlock, K. Rutledge, K. Stamnes, and Y. Wang, "Analytical solution of radiative transfer in the coupled atmosphere-ocean system with a rough surface," *Appl. Opt.*, vol. 45, no. 28, pp. 7443–7455, 2006.
- [50] J. Fraden, "Handbook of modern sensors: Physics," in *Designs, and Applications Handbook of Modern Sensors*. New York, NY, USA: Springer-Verlag, 2003.
- [51] D. Rankin, D. D. Kekez, R. E. Zee, F. M. Pranajaya, D. G. Foisy, and A. M. Beattie, "The CanX-2 nanosatellite: Expanding the science abilities of nanosatellites," *Acta Astronaut.*, vol. 57, no. 2, pp. 167–174, 2005.
- [52] J. J. Puscell and P. Masini, "Uncooled emissive infrared imagers for CubeSats," *Proc. SPIE*, vol. 9223, pp. 922307-1–922307-7, Sep. 2014.
- [53] K. P. Thompson and J. P. Rolland, "Freeform optical surfaces: A revolution in imaging optical design," *Opt. Photon. News*, vol. 23, no. 6, pp. 30–35, 2012.
- [54] J. P. Angel, N. J. Woolf, and H. W. Epps, "Good imaging with very fast paraboloidal primaries: An optical solution and some applications," in *Proc. Astron. Conf.*, 1982, pp. 134–140.
- [55] K. A. Sinclair, "Design and test of a slab waveguide spectrometer for spatial heterodyne observations of water vapor," Ph.D. dissertation, Earth Space Sci. Program, York Univ., Toronto, ON, Canada, 2014.
- [56] M. W. McElwain *et al.*, "Scientific design of a high contrast integral field spectrograph for the subaru telescope," *Proc. SPIE*, vol. 8446, p. 84469C, Oct. 2012.
- [57] H. Yuan *et al.*, "FPA development: From InGaAs, InSb, to HgCdTe," *Proc. SPIE*, vol. 6940, p. 69403C, Sep. 2008.
- [58] C. K. Gatebe, J. J. Butler, J. W. Cooper, M. Kowalewski, and M. D. King, "Characterization of errors in the use of integrating-sphere systems in the calibration of scanning radiometers," *Appl. Opt.*, vol. 46, no. 31, pp. 7640–7651, 2007.
- [59] S. Grabarnik, M. Taccola, L. Maresi, V. Moreau, L. de Vos, J. Versluys, and G. Gubbels, "Compact multispectral and hyperspectral imagers based on a wide field of view TMA," in *Proc. Int. Conf. Space Opt.*, vol. 4, Rhodes, Greece, 2010, p. 8.



Tilak Hewagama is a Researcher at the University of Maryland, where he is working in the Planetary Systems Laboratory (693), NASA GSFC. Research areas include composition, dynamics, and thermal structure of solar system planets, solar physics, molecular spectroscopy, and exoplanets. He is also involved in developing UV/visible/IR spectroscopy and radiometry instruments for remote sensing, and SmallSat/CubeSat missions for solar system exploration.



Georgi T. Georgiev received the Diploma degree in engineering from the Budapest Technical University, Budapest, Hungary, and the Ph.D. degree in optical physics from the Bulgarian Academy of Sciences, Sofia, Bulgaria. He was with the University of Maryland, where he worked on NASA GSFC projects on acousto-optic imaging spectroscopy. He is currently with the NASA Langley Research Center, Hampton, VA, USA, supporting radiometric calibration of remote sensing projects. His current research interests include the calibration and characterization of remote sensing instruments from the ultraviolet through the microwave, optical metrology, radiometry, remote sensing, and the measurement of reflective and transmissive optical scatter.



Bert Pasquale is currently a Senior Optical Designer with the NASA Goddard Space Flight Center, Greenbelt, MD, USA. He currently serves as the Optical Design Group Leader with the Instrument Systems and Technology Division, and is an Optical Design and Analysis Lead for WFIRST, NASA's next Hubble-class great observatory.



Shahid Aslam received the D.Phil. degree in physics from the University of Oxford in 2006. He is currently a Space Scientist at NASA Goddard Space Flight Center, MD, USA, where he is developing new technology for space remote sensing instrumentation, including CubeSats and SmallSats for solar system planets. He is currently the CIRS Instrument Scientist on the Cassini Mission. He has published more than 45 peer reviewed papers and holds three U.S. Patents. Dr. Aslam was a recipient of the NASA Public Service Award Medal for his contributions in GaN sensing technology.



Sreeja Nag received the S.M. degree in aeronautics and astronautics, the S.M. in technology and policy, and the Ph.D. degree in space systems (engineering) from the Massachusetts Institute of Technology. She is currently a Senior Research Scientist with the NASA Ames Research Center, Bay Area Environmental Research Institute, and also with the NASA Goddard Space Flight Center. She is also a principal investigator or co-investigator in several NASA funded grants in the areas of systems engineering, constellations, and formation flight for Earth observation.



Charles K. Gatebe works with the Universities Space Research Association based at NASA Goddard Space Flight Center, Climate and Radiation Laboratory. He is group lead and the principal investigator of NASA's Cloud Absorption Radiometer (CAR) instrument. Dr. Gatebe is a leader in the airborne measurements and analysis of surface bidirectional reflectance distribution function. He has received many awards including the prestigious Robert H. Goddard Award for Outreach and the World Meteorological Organization Young Scientist Award.